Probing DAMOCLES: Testing and a Parameter Sensitivity Analysis

The introduction of any new piece of software into a field has the potential to yield exciting new results. The first step in this process should therefore be a thorough investigation into the reliability of the code and an assessment of the outputs from a theoretical standpoint. Before the modelling of real data takes place, it is important to understand why the variation of a given parameter affects results in a particular way. A comprehensive understanding of parameter space not only facilitates the modelling process but may also give rise to interesting results in and of itself.

To this end, this chapter describes the ways in which DAMOCLES was tested and the results of these tests. I then also present a parameter sensitivity analysis. I describe the changes that are seen in the shapes of line profiles and consider any distinctive features that arise as a result of varying the parameters of interest. I also contemplate the physical processes behind these effects.

3.1 Testing and benchmarking the code

The field of astronomy is highly reliant on the production of bespoke software to understand and interpret observations from telescopes and to develop and test new theories. As one of only a few sciences which do not have the ability to run experiments or to vali-

date results in a laboratory, progress is made via mathematical analyses or computational models based on observed data. Astrophysicists typically develop their own programs because a deep understanding of the topic to be modelled is required. Like any experiment, however, the "apparatus" should be checked and tested in order to establish its reliability.

Throughout the production of DAMOCLES, I sought, as far as was possible, to maintain best practices in scientific computing as detailed by Wilson et al. (2012). The code is carefully structured into modules and subroutines as described in the previous chapter. Each of these units was inspected for sense and accuracy as it was written, and at each update and addition the code as a whole was tested against basic logical checks, for example comparing outputs to manually calculated properties. In addition to regular evaluations conducted throughout the program development, it was very important to establish that DAMOCLES produced standard results as expected.

There is a general lack of published models in the literature that consider dust-affected asymmetric line profiles. This is problematic since there are no published benchmark cases against which I could compare results. I therefore considered a number of analytic line profiles derived from first principles for the case of a dust-free spherically symmetric expanding medium. This process ensured the functionality of the grid and the initialisation and propagation of energy packets. Additionally, I also checked the the absorption and scattering components of the code which are crucial to the modelling of a dusty medium. I considered some optically thick scenarios and qualitatively compared my results with those derived by Lucy et al. (1989). The profiles presented by Lucy et al. (1989) are produced both analytically and from numerical modelling and are of scenarios that are typical of those treated by DAMOCLES. They are also the only published numerical models of dust-affected asymmetric line profiles and as such it is important that DAMOCLES is capable of reproducing these results.

3.1.1   Theoretical line profiles from first principles

The simple nature of a spherically-symmetric expanding medium with a given velocity outflow law and emissivity distribution allows for analytical line profiles to be calculated from first principles in the dust-free case. Based on the methods of Gerasimovic (1933), I derive a set of three equations that describe the contours of theoretical line profiles under different starting conditions.

Describing the fractional expansion velocity of the shell as $v(r) \propto r^\alpha$ with $\alpha \neq 0$ such
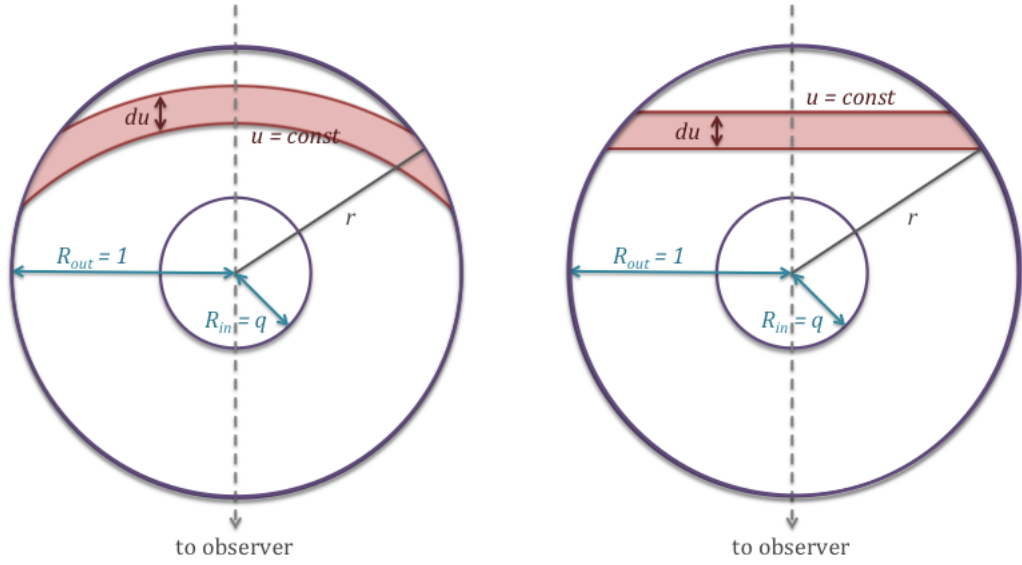
Figure 3.1. Diagrams illustrating the dust-free model and some of the relevant variables used in the derivation of the equations of analytical line profiles. On the left is the general case with curves of constant u labelled. On the right is the special case of an orthogonal (u, s) net when $\alpha = 1$ and therefore $v(r) \propto r$.

that $v(r) = \frac{V(r)}{V_{max}}$ where $V(r)$ and V_{max} represent physical velocities and $v_{max} = 1$, the velocity along the line-of-sight to the observer is given by

$$u(r, \theta) = r^\alpha \cos \theta \tag{3.1}$$

For curves with constant line-of-sight velocity $u = const$ we therefore have

$$dr = \frac{r}{\alpha} \tan \theta \, d\theta \tag{3.2}$$

For $u = const$, the line element ds is given by

$$ds^2 = r^2 \, d\theta^2 + dr^2 = r^2 \left(\frac{\tan^2 \theta}{\alpha^2} + 1 \right) d\theta^2 \tag{3.3}$$

and therefore, along curves of constant u we have

$$s = u^{\frac{1}{\alpha}} \int_{\theta_0}^{\theta_1} \frac{\sqrt{\frac{\tan^2 \theta}{\alpha^2} + 1}}{\cos^{\frac{1}{\alpha}} \theta} \, d\theta \tag{3.4}$$

The angle ψ between the tangent to a curve and the radial line is given by the formula

(in polar coordinates)

$$\tan \psi = r \frac{d\theta}{dr} \qquad (3.5)$$

which for curves of $u = const$ gives

$$\tan \psi = \frac{\alpha}{\tan \theta} \qquad (3.6)$$

Curves of constant line-of-sight velocity therefore intersect the line $\theta = 0$ orthogonally, although the (u, s) net is only orthogonal if $\alpha = 1$ (see Figure 3.2).

We can now construct a volume element between u and $u + du$ by rotating a section of thickness du around the $\theta = 0$ axis. Assuming that $i(r)$ is the emission per unit volume (dependent only on radius), then the energy emitted by the nebula between u and $u + du$ is proportional to

$$\int_{\mathcal{C}} i(r) \; r \sin \theta \; r \, d\theta \, dr \;\; = \;\; \int_{\mathcal{C}'} [i(r) \; r^2 \sin \theta] \; \frac{\partial(r, \theta)}{\partial(u, s)} \, ds \, du \qquad (3.7)$$

where the integral is a line integral along curves $\mathcal{C}$ of constant u and square brackets denote a change of variables.

We therefore compute the Jacobian from Equations 3.1 and 3.4 as

$$\frac{\partial(u, s)}{\partial(r, \theta)} \;\; = \;\; \alpha u \sqrt{\frac{\tan^2 \theta}{\alpha^2} + 1} \qquad (3.8)$$

Assuming an initial emissivity distribution dependent on radius only, we put $i(r) \propto r^{-2\beta}$ (i.e. appropriate for a gas density distribution $\rho \propto r^{-\beta}$ with the emissivity proportional to the gas density squared). Substituting Equation 3.8 into Equation 3.3 and calculating the curvilinear integral along curves of constant u yields the following:

$$i(u) \, du \;\; \sim \;\; du \int_{\mathcal{C}} \frac{r^{2(1-\beta)} \sin \theta}{\alpha u \sqrt{\frac{\tan^2 \theta}{\alpha^2} + 1}} \, ds \qquad (3.9)$$

Substituting in Equations 3.1 and 3.7 and transforming to an integral in θ gives

$$
\begin{aligned}
i(u)\, du &\sim \frac{du}{\alpha u^{\frac{2\beta-3+\alpha}{\alpha}}} \int_{\theta_0}^{\theta_1} \cos^{\frac{2\beta-3}{\alpha}} \theta \sin\theta\, d\theta \\
&\sim \frac{du}{u^{\frac{2\beta-3+\alpha}{\alpha}}} \left[\frac{\cos^{\frac{2\beta-3+\alpha}{\alpha}} \theta}{2\beta-3+\alpha} \right]_{\theta_0}^{\theta_1}
\end{aligned}
\tag{3.10}
$$

for $\frac{2\beta-3}{\alpha} \neq -1$ where $i(u)\, du$ is the energy emitted in a volume element and θ_0 and θ_1 are the bounds of this element. The case $\frac{2\beta-3}{\alpha} = -1$ results in a logarithmic relationship.

In the case of a "filled" nebula, i.e. one where the inner radius is vanishingly small in comparison to the outer radius the above result may be evaluated between $\theta_0 = 0$ and $\theta_1 = \arccos u$ and the equation of the line profile is

$$
i(u)\, du \sim \pm \frac{du}{(2\beta-3+\alpha)u^{\frac{2\beta-1+\alpha}{\alpha}}} \left(1 - u^{\frac{2\beta-3+\alpha}{\alpha}} \right)
\tag{3.11}
$$

If the nebula is not "filled", that is to say, the inner radius is some fraction of the outer radius and the remnant is a detached shell with inner radius $R_{in} = q$ and outer radius $R_{out} = 1$ such that $q = \frac{R_{in}}{R_{out}}$, the above formula is only valid from some critical value $u' = q^\alpha$ to $u = 1$. For $u < u'$, we obtain

$$
i(u)\, du \sim \pm \frac{du}{(2\beta-3+\alpha)} \left(\frac{1}{q^\alpha} - 1 \right)
\tag{3.12}
$$

and therefore the top of the line is flat while the sides are sloping.

Crucially, the width of the flat section is determined by

$$
u' = q^\alpha
\tag{3.13}
$$

or simply $u' = q$ in the case where $v \propto r$, whilst the shape of the profile outside of the flat-topped region is described by Equation 3.11.

Profiles with a variety of shapes may be derived from these formulae depending on the relative values of α and β. Here we consider three main families of curves:

1. $i(u) \sim u^{-\gamma} - 1 \quad (\alpha > 0,\ 2\beta - 3 + \alpha > 0)$

2. $i(u) \sim 1 - u^\gamma \quad (\alpha > 0,\ 2\beta - 3 + \alpha < 0)$

3. $i(u) \sim -\log u \quad (\alpha > 0,\ 2\beta - 3 + \alpha = 0)$
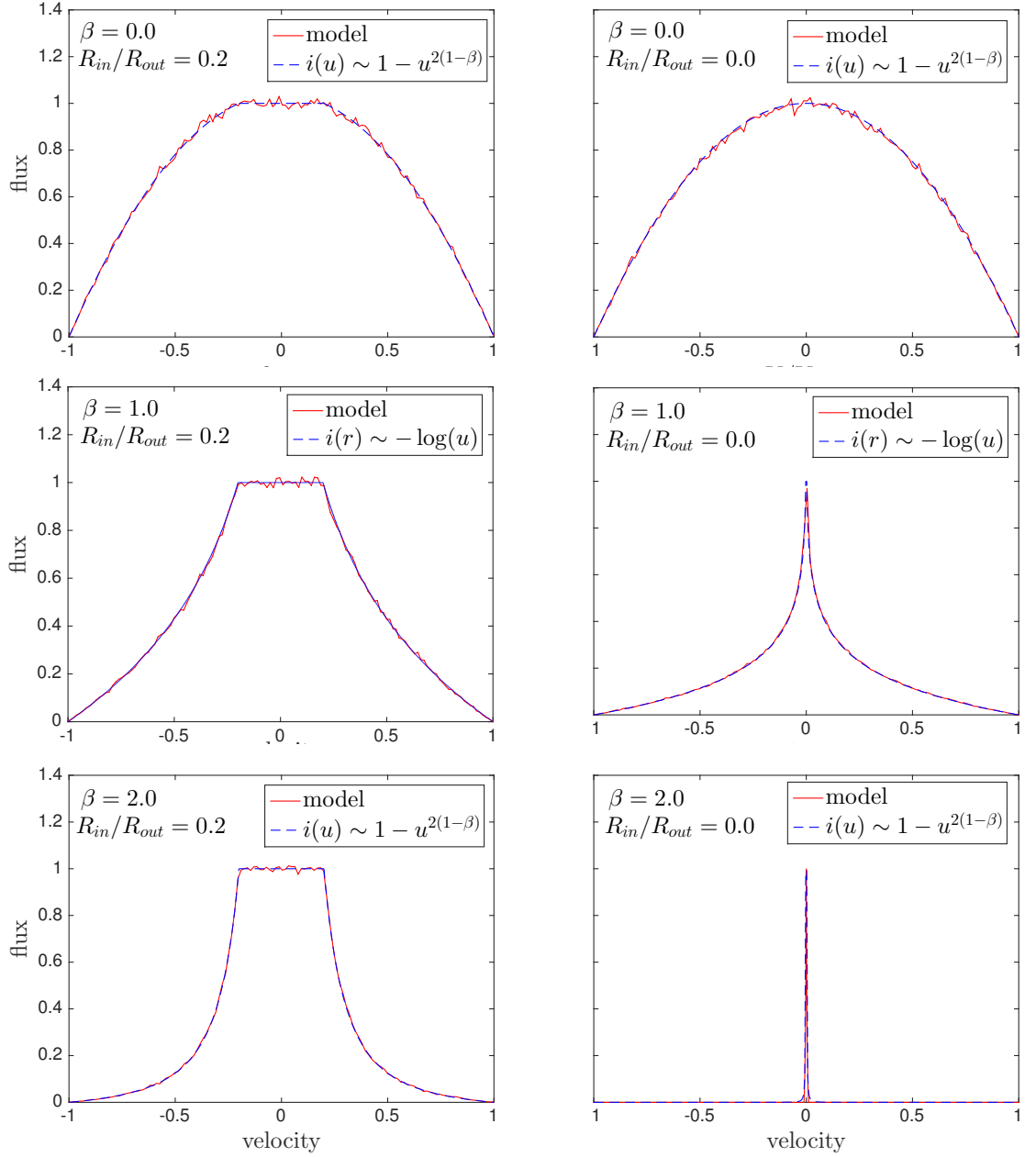
Figure 3.2. *Red:* Benchmark models for optically thin ($\tau = 0$) line profiles with fractional velocity $v(r) \propto r$. Top to bottom: initial emissivity profiles $i(r) \propto r^{-2\beta}$ with $\beta = 0.0$, $\beta = 1.0$ and $\beta = 2.0$. Cases with $R_{in}/R_{out} = 0.2$ are on the left and $R_{in}/R_{out} = 0.0$ on the right. The presence of a plateau in the upper plots is due to the finite inner radius (detached shell). *Blue:* The analytical case with $i(u) \sim 1 - u^{2(1-\beta)}$ except in the case of $\beta = 1$ where $i(u) \sim -\log u$.
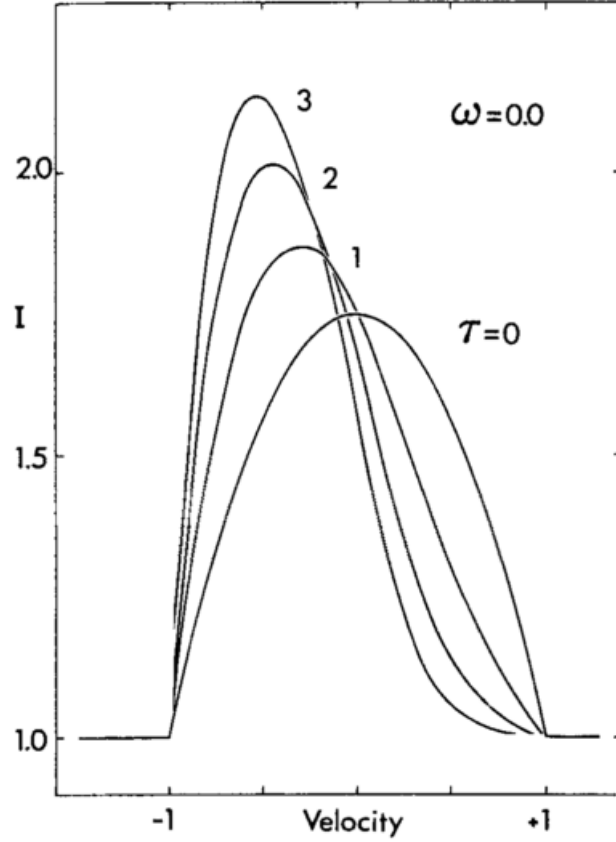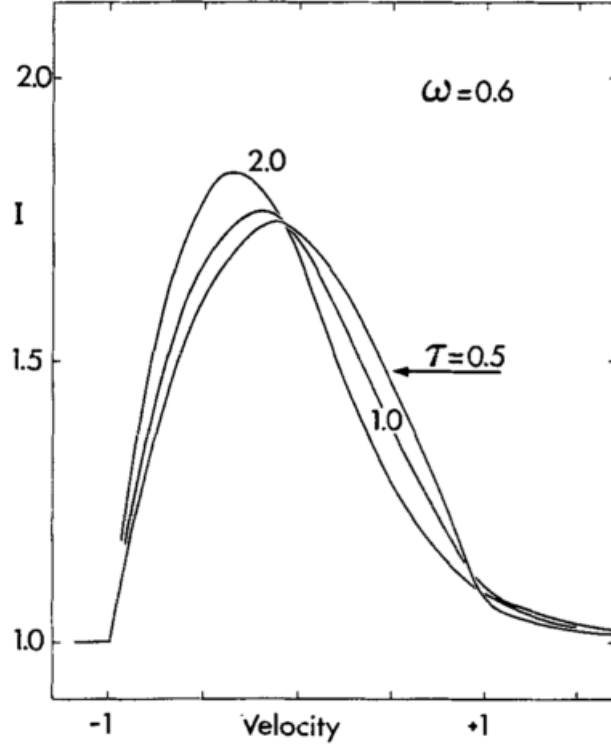
Figure 3.3. The analytically derived line profiles of (Lucy et al. 1989) corresponding to their Model II scenario with zero albedo dust for a variety of total dust optical depths.

where γ is defined as $\gamma = |\frac{2\beta-3+\alpha}{\alpha}|$.

Models are presented for each of these cases, both for a filled nebula and for a shell structure with $R_{in}/R_{out} = 0.2$. A velocity profile $v \propto r$ appropriate for supernova ejecta in the free expansion phase is used throughout (Li & McCray 1992; Xu et al. 1992; McCray 1996; Baron et al. 2005). Values of $\beta = 0, 1$ and 2 are adopted. Figure 3.2 illustrates the excellent agreement between the analytical case and the models. All fluxes are scaled to unity at the peak.

I conclude from this testing that all aspects of the code that are associated with initialising the packets into the grid are functioning correctly since an error at this stage would result in disagreement with the above theory.

Figure 3.4. The numerically modelled line profiles of (Lucy et al. 1989) corresponding to their Model III scenario with dust of albedo $\omega = 0.6$ for a variety of total dust optical depths.

3.1.2 Benchmarking against numerical models

In addition to the tests for the optically thin line profiles detailed above, I also compared my outputs to those derived by Lucy et al. (1989) in order to assess the accuracy of the scattering and absorption aspects of the code. I considered two similar cases, equivalent to Models II and III of Lucy et al. (1989) (see Figures 3.3 and 3.4 respectively). In the first case, dust with zero albedo (pure absorption) was uniformly distributed throughout a filled nebula with a velocity profile $v \propto r$. In the second case, the same scenario was considered but in a medium of dust with albedo $\omega = 0.6$.

In the first case, the profile may once again be derived analytically from the basic geometry using the fact that radiation will be attenuated by a factor $e^{-2\tau_\nu v}$ between points with line-of-sight fractional velocities $-v$ and $+v$ where τ_ν is the optical depth at frequency ν from the centre to the outer edge of the ejecta. The line profile is therefore

given by

$$\frac{I(v)}{I(-v)} = \exp(-2\tau_\nu v) \qquad (3.14)$$

Lucy et al. (1989) presented several examples for both the analytical case of the perfect absorber and a Monte Carlo model for grains with albedo $\omega = 0.6$. I include their profiles here for comparison in Figures 3.3 and 3.4. I present line profiles in Figure 3.5 that were generated by DAMOCLES using the same model parameters as described by Lucy et al. (1989). I note that the resulting profiles exhibit the same features and shape. The peaks of all profiles are shifted further to the blue with increasing optical depth and all profiles are also flux-biased towards the blue. Of particular interest is the scattering wing that appears beyond the maximum velocity ($v_{max} = 1$) on the red side of the profiles in the partial scatterer case as a result of the packets doing work on the expanding sphere. This was noted by Lucy et al. (1989) as a potential diagnostic for the presence of dust in the ejecta of a supernova and I will discuss this further in the next section.

3.2 A Parameter Sensitivity Analysis

It is of general interest to establish potential diagnostic signatures in the line profiles of supernovae and their remnants in order to trace dust formation more effectively. The capacity to specify a number of parameters is included in DAMOCLES. The variation of each parameter potentially affects the contour of the resulting line profile in a different way. By investigating each parameter separately over a range of values whilst keeping the other parameters fixed, it may be possible to identify certain characteristics of dust-affected line profiles that may be associated with a particular property of the dusty medium. This insight could help to explain unusual or interesting features of observed line profiles where dust is suspected to be an influential factor. In this chapter, I investigate and discuss the effects of the main parameters of interest, namely:

- the maximum velocity, V_{max}

- the ejecta radius ratio, R_{in}/R_{out}

- the dust optical depth, τ
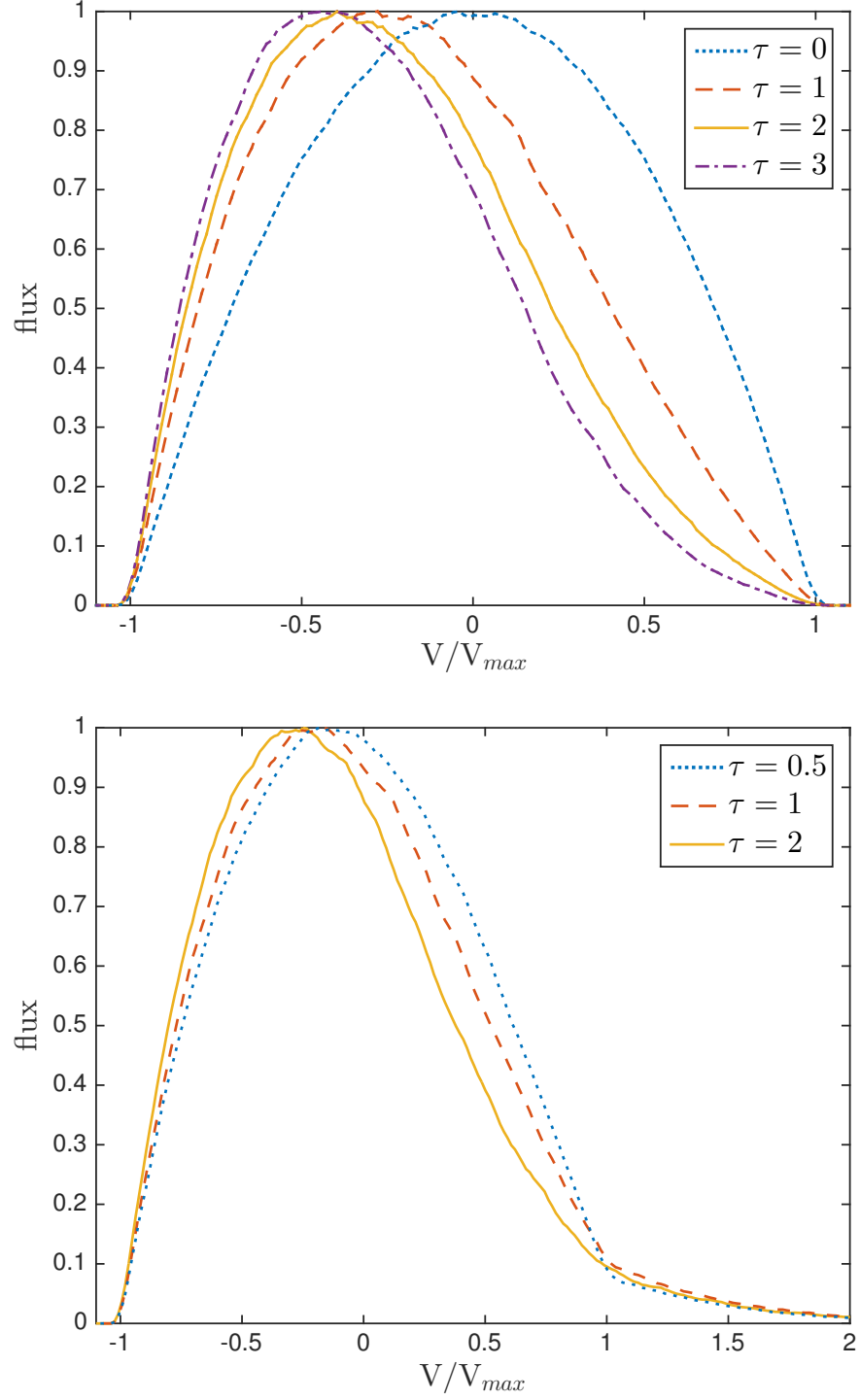
Figure 3.5. Benchmark models for line profiles with $v \propto r$, $i(r) \propto$ constant and a filled sphere with $R_{in}/R_{out} = 0$. Pure dust absorption models ($\omega = 0$) are presented in the top plot, whilst partially scattering models are presented at the bottom ($\omega = 0.6$) as per Lucy et al. (1989) Models II and III. All resulting profiles have been scaled to unity flux at their peaks.

- the dust albedo, ω

- the dust density profile exponent, β, where $\rho \propto r^{-\beta}$

I also investigate the capacity of this type of model to infer properties of the dust itself, specifically the dust grain radius range and distribution, and the variety and relative abundances of different species present in the dusty medium.

3.2.1 The maximum line velocity, V_{max}

The maximum velocity is defined as the velocity at the outer edges of the line emitting region for a given line. The maximum velocity may vary between different spectral lines or doublets due to different locations of species having differing ionization thresholds. Clearly, the larger the maximum velocity used the wider the profile becomes. To some extent therefore the steepness of the density profile and the maximum velocity can act to counter each other since a steeper density distribution narrows the profile (see Section 3.2.5). The shape of the wings of the profiles, however, generally precludes much degeneracy in this aspect - the overall shape of the line profile can be used to determine the exponent of the density distribution to within a relatively small range.

More important is the effect that the maximum velocity has on the overall optical depth. Since the outer radius is calculated directly from the maximum velocity (as $R_{out} = V_{max} \times t$ where V_{max} is determined from the blue side of the observed line profile), the overall volume of the ejecta is determined solely by this value and the ratio of the inner and outer radii. The total dust optical depth to which the radiation is exposed can therefore be greatly affected by even a relatively small change in the maximum velocity for fixed values of the other parameters. Practically, however, the maximum velocity can usually be fairly well determined from the observations (identified as the point where the flux vanishes on the blue side) and may be further constrained through modelling.

3.2.2 The ejecta radius ratio, R_{in}/R_{out}

As already discussed in Section 3.1.1, the width of the flat top is determined by the ratio of the inner and outer radii, the exponent of the velocity profile and the maximum velocity. I assume that the supernova is in free expansion from just a few months after the explosion and therefore $r = vt$ such that within the ejecta the velocity profile takes the form $v \propto r$

at a fixed time i.e. the supernova expands self-similarly (Li & McCray 1992; Xu et al. 1992; Kozma & Fransson 1998b). For this case, R_{in}/R_{out} is given by

$$\frac{R_{in}}{R_{out}} = \frac{V_{min}}{V_{max}} \tag{3.15}$$

where it is often possible to constrain V_{min} and V_{max} to a relatively narrow range simply from the observed line profile.

The majority of spectral lines emitted from supernovae and supernova remnants are expected to have a flat top before dust attenuation effects since it is rare for these objects to form a completely filled nebula. However, even a very small amount of dust attenuation may result in the line profile appearing to be smoothed at its peak.

The effects of absorption by dust on a line profile for a filled nebula with $R_{in}/R_{out} = 0$, as opposed to a detached shell, are shown in Figure 3.5. All profiles have been scaled to unit flux at their peaks.

3.2.3   The dust optical depth, τ

As expected, greater attenuation of the original line profile is seen on the red side (see Figures 3.7 and 3.6). The profiles are most revealing at lower dust optical depths since the effects of the asymmetric absorption can be seen in different sections of the profiles and the profiles therefore tend to exhibit more features. The region of the profile that is most clearly affected by dust absorption is the flat-topped region. A small amount of absorption in this region results in a skewed profile, with a fraction of the flat-topped section removed. The peak becomes blue-shifted as a result, but only to the original value of $-V_{min}$, the minimum velocity corresponding to R_{in}. In addition to the attenuation in this region, the red wing of the profile is also somewhat reduced, and the blue wing somewhat increased relative to their original symmetric positions. The result is a relatively "jagged" looking profile, often with sharp changes at $\pm V_{min}$. The profile is generally asymmetric, although the degree of absorption in the flat-topped region may sometimes make it seem as though the profile is in fact symmetric and uniformly blue-shifted (see Section 3.2.7 for further discussion). Observationally, these sharp features might become smoothed due to insufficient spectral resolution.

At high dust optical depths or when the ratio of the inner and outer radii is small,
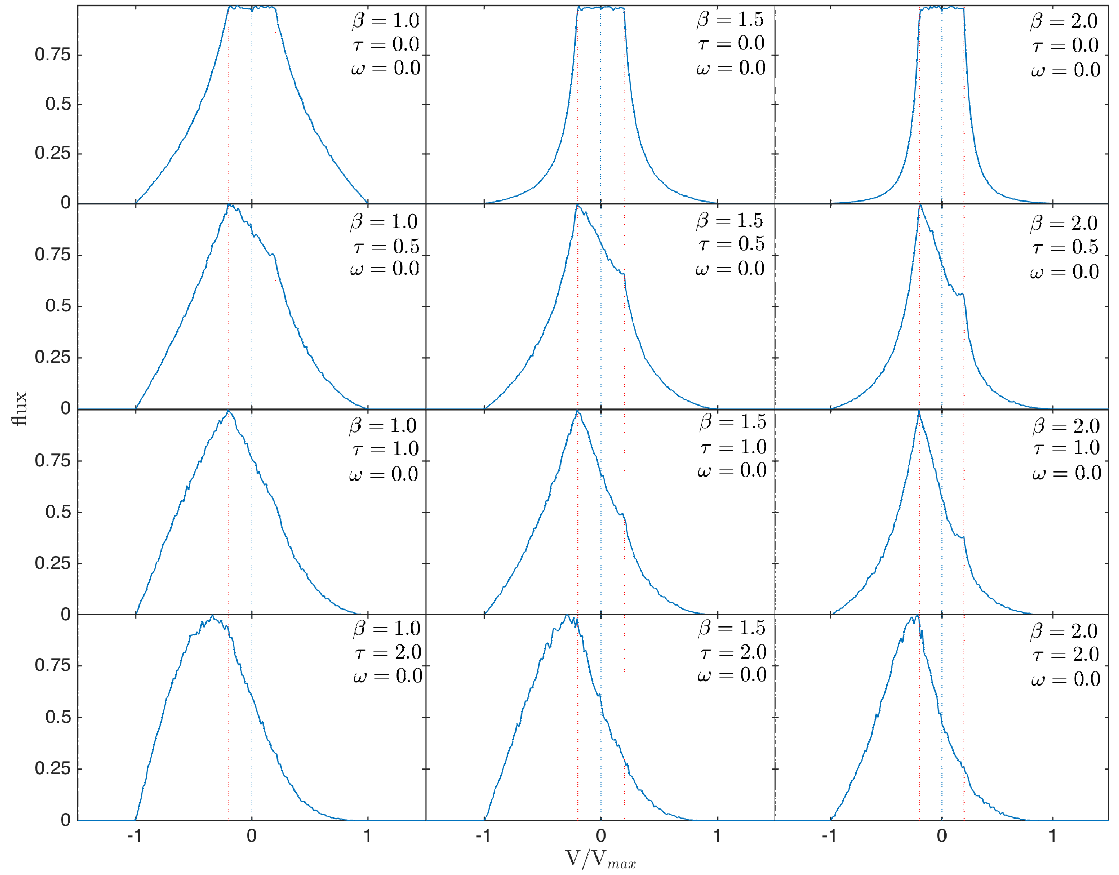
Figure 3.6. Set of models with $i(r) \propto r^{-2\beta}$ for $\beta = 1.0$ (left), $\beta = 1.5$ (middle) or $\beta = 2.0$ (right), $\omega = 0$, $R_{in}/R_{out} = 0.2$, $v(r) \propto r$ and $v_{max} = 1$ illustrating the effects of varying τ. Peak fluxes are scaled to unity.

the entire profile is shifted to the blue and the peak moves beyond $-V_{min}$ further into the blue. The profiles also tend to become more smooth and featureless. A set of models showing the effects of varying optical depths for different density profiles and dust albedos are presented in Figures 3.7 and 3.6 with $R_{in}/R_{out} = 0.2$.

The complete nebula case

To reproduce similar characteristic dust-affected line profiles where the peak of the profile is shifted beyond $-V_{min}$ into the blue is "easier" for smaller values of V_{min}. The complete nebula is therefore effectively analogous to cases of higher optical depths for a detached shell and the same effects that are illustrated in Figures 3.6 and 3.7 apply.
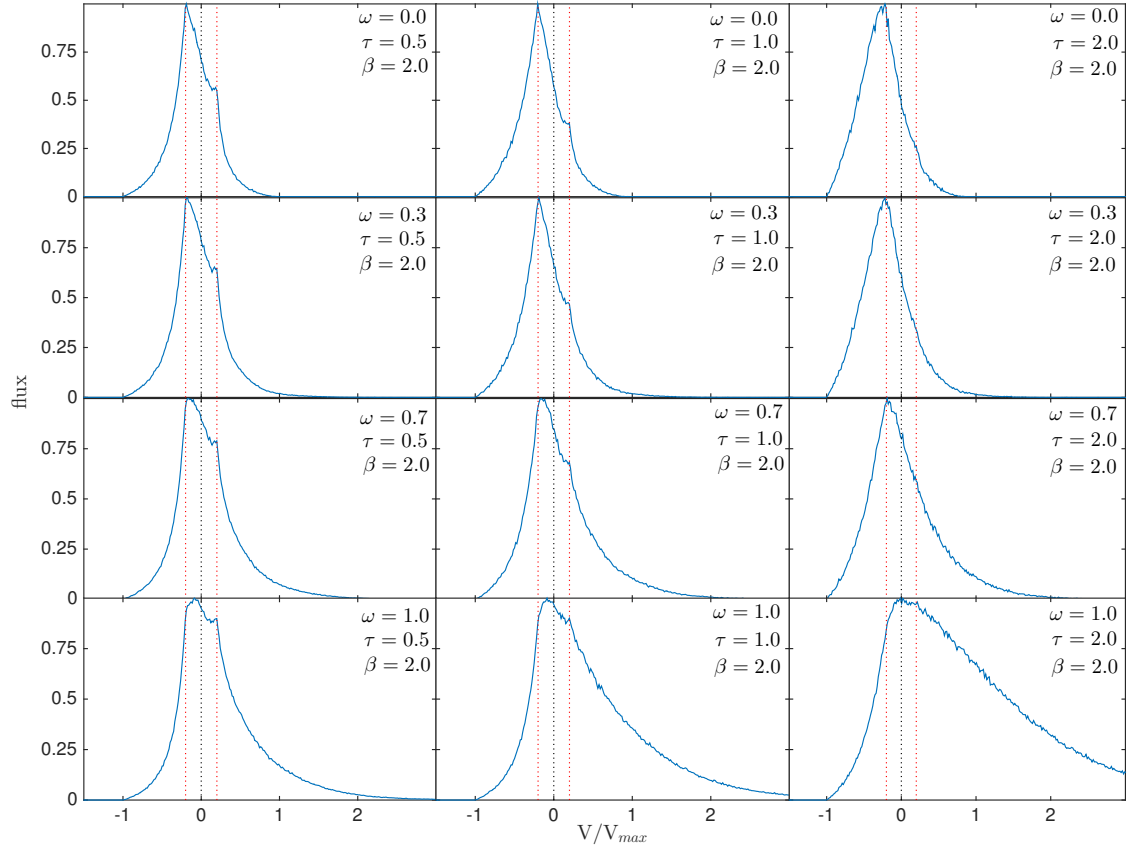
Figure 3.7. Set of models with $i(r) \propto r^{-4}$ (i.e. $\beta = 2.0$), $R_{in}/R_{out} = 0.2$, $v(r) \propto r$ and $v_{max} = 1$ illustrating the effects of varying τ and ω. Peak fluxes are scaled to unity.

3.2.4 The dust albedo, ω

In the past, there has often been a focus on the effects of absorption by dust on the shapes of line profiles and less attention has been paid to the potential effects of scattering by dust. In fact, line profiles can be significantly affected by scattering of radiation. The greater attenuation of radiation received from the receding portion of the ejecta results in an asymmetry of the line profile whereby the majority of the observed emission is located bluewards of the peak. However, the effects of repeated dust scattering events within the ejecta can substantially alter the shape of a line profile and potentially can act to counter the blue-shifted asymmetry.

Not only does repeated scattering of photons increase the number of potential opportunities for a given photon to be absorbed but it also results in continuous shifting of the frequency of the photon to the red. The photon must do work on the expanding shell of dust in order to escape and thus many of the photons are reprocessed beyond the theoret-

ical maximum velocity on the red side of the profile. Even in the case of dust grains with a relatively low albedo, a surprisingly persistent wing on the red side of the profile is seen, generally beyond the maximum theoretical velocity of the emitting region. In the case of strong dust scattering and high dust optical depths, this can actively result in a shift in the overall asymmetry of the profile, with the majority of the emission being emitted redwards of the peak. The peak however, remains blue-shifted (for example the bottom left panel of Figure 3.7) or central (for example the bottom right panel of Figure 3.7). For the line profile to exhibit this effect requires the dust to be a nearly perfect scatterer; of the albedos plotted in Figure 3.9 only the nearly-transparent $MgSiO_3$ sample of Jäger et al. (2003) exhibits such a behaviour.

The combination of relatively low dust optical depths, initially flat-topped profiles, greater attenuation on the blue side along with increased flux on the red side due to scattering can result in a profile that sometimes ends up appearing almost symmetrical, particularly if contaminants, such as narrow lines or blending with other broad lines, are present or if the resolution of the data is low. The potential for apparently symmetrical profiles that appear to have been uniformly blue-shifted should be noted (see Figures 3.7 and 3.6 for examples of this).

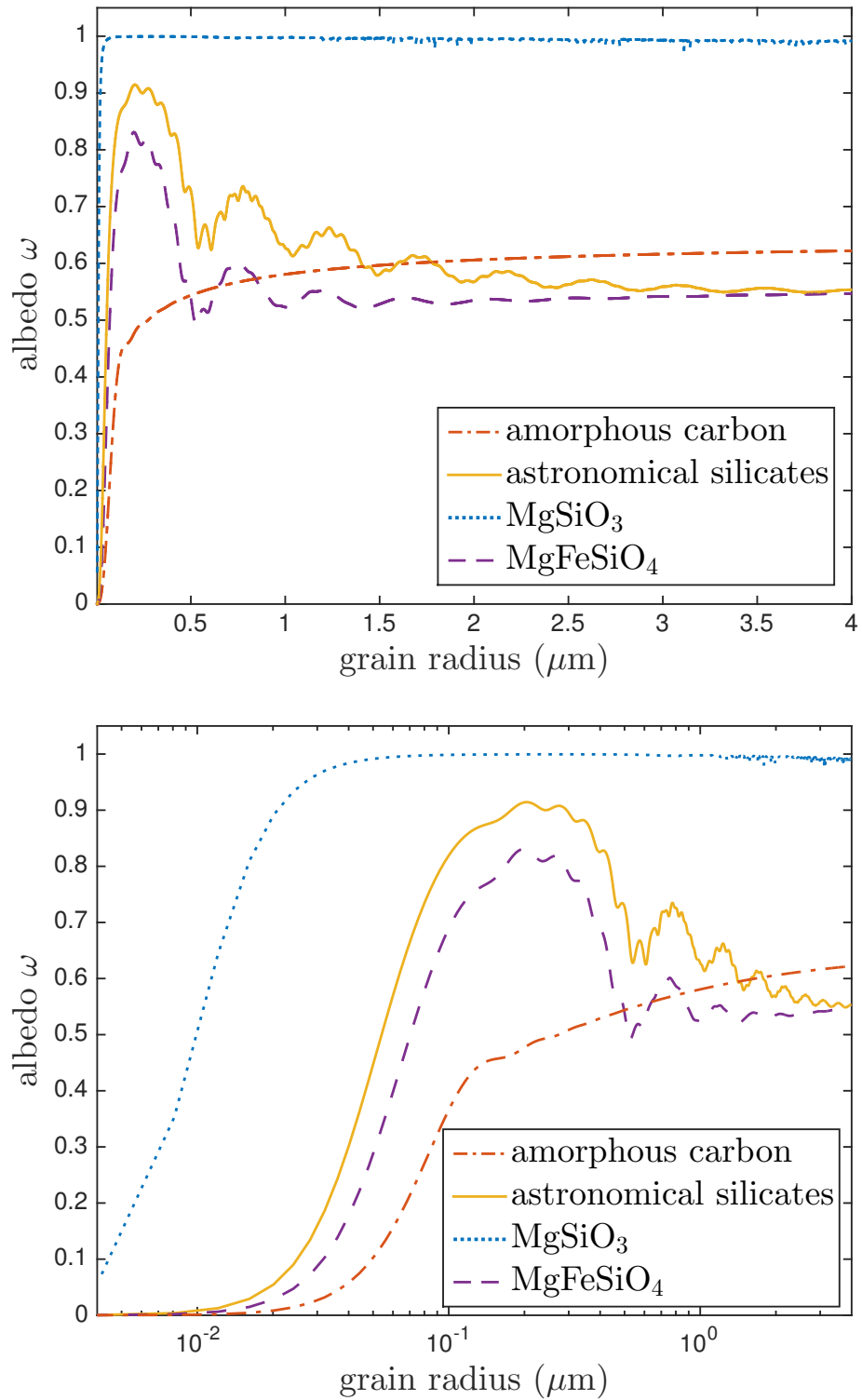### 3.2.5 The dust density profile, $\rho \propto r^{-2\beta}$

Whilst the density profile of the dust may have some effect on the resulting profiles, it is the initial emissivity profile (dependent on the gas density profile) that has the greatest effect on the shape of the line profile. In general, the steeper the emissivity distribution, the narrower the line profile becomes. The sides of the line profile may become almost vertical for a very steep distribution since the majority of the emission then comes from a very narrow velocity range (see Figure 3.2). For a flat-topped profile of fixed width this approximates the square profile produced in the case of an emitting shell with constant velocity.

The dependence of the shape of the line profile on the emissivity distribution is described analytically in Section 3.1.1 for the case of very optically thin dust. However, for even fairly low dust optical depths, the density profile plays a significant role in determining the shape of the line profile where it is affected by dust absorption. As previously discussed, at relatively small optical depths for reasonable R_{in}/R_{out}, a section of the flat-topped region is removed resulting in a peak at $-V_{min}$. The shape of the profile in this
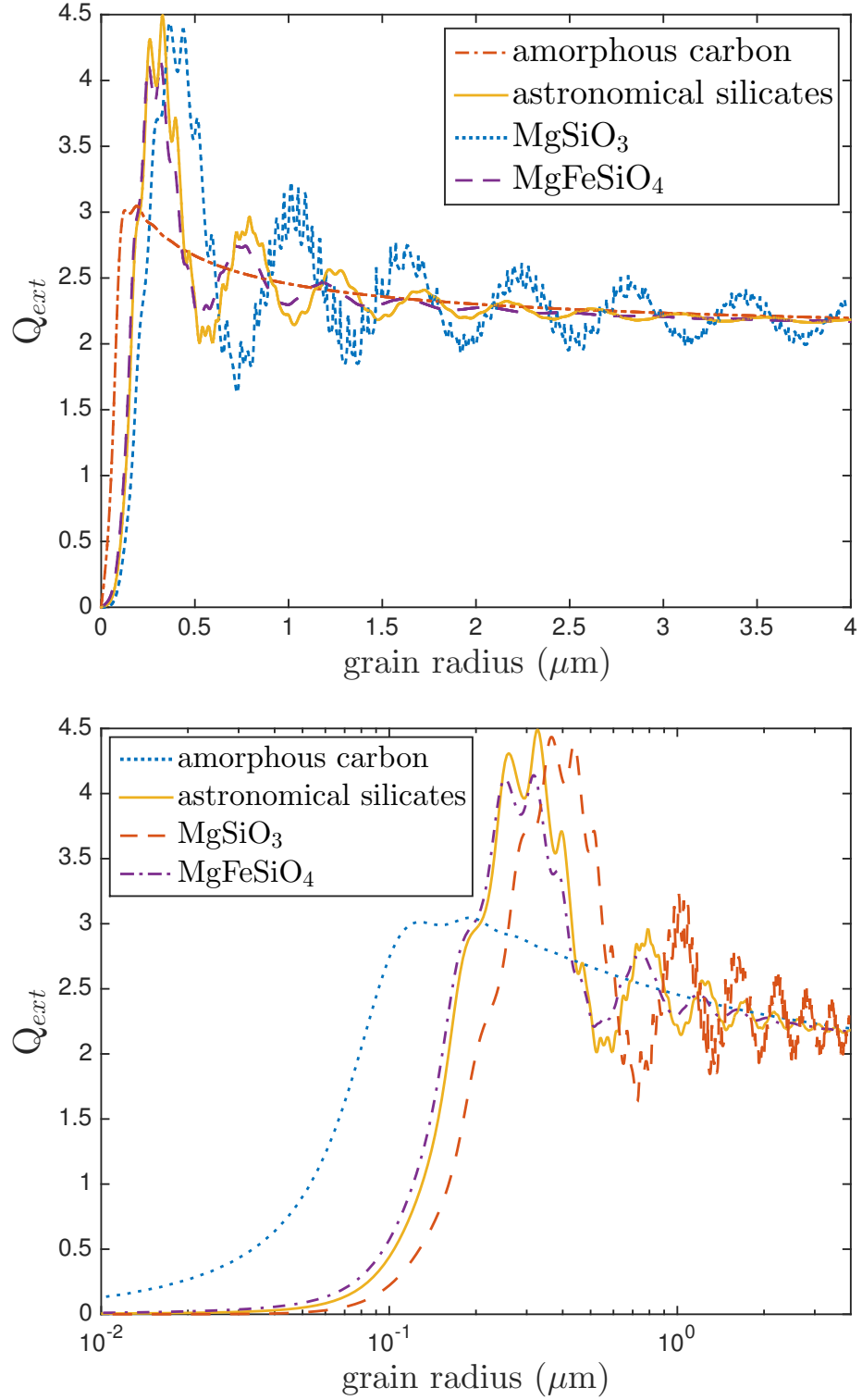
Figure 3.8. The variation of extinction efficiency (Q_{ext}) with grain radius at λ = 656 nm for Zubko et al. (1996) BE amorphous carbon, Draine & Lee (1984) astronomical silicate and the MgSiO$_3$ and MgFeSiO$_4$ samples of Jäger et al. (2003) and Dorschner et al. (1995) respectively. A linear scale is presented on the top and a log scale on the bottom.

Figure 3.9. The variation of albedo with grain radius at $\lambda = 656$ nm for Zubko et al. (1996) BE amorphous carbon, Draine & Lee (1984) astronomical silicate and the $MgSiO_3$ and $MgFeSiO_4$ samples of Jäger et al. (2003) and Dorschner et al. (1995) respectively. A linear scale is presented on the top and a log scale on the bottom.

region is significantly affected by the density profile. Shallow density profiles (low β) produce a virtually linear variation in flux between $-V_{min}$ and $+V_{min}$ (for example the profiles in the left column of Figure 3.6). For a fixed dust optical depth, the steeper the distribution becomes, the more concave the profile becomes between $-V_{min}$ and $+V_{min}$, ultimately resulting in a clear shoulder to the profile at $+V_{min}$ (for example the profiles in the right column of Figure 3.6). For extremely steep density distributions this can result in a double peaked profile with a trough to the red of $V = 0$. An illustration of the effects on the line profiles of varying β and τ is shown in Figure 3.6. As previously noted, these features may not be apparent in observed line profiles with poor spectral resolution.

### 3.2.6 Inferring properties of the dust from the models

The presence of an extended red wing at large positive velocities in combination with increased extinction on the red side at smaller positive velocities can allow the values of τ and ω to be well constrained. Where this occurs it is possible to translate these values into a dust mass and grain radius for a given species or combination of species using grain optical properties and Mie theory (see Figure 3.9).

For amorphous carbon, the albedo generally increases with grain radius. The presence and extent of any scattering wing on the red side of the observed profile can therefore help to place limits on the grain radius. However, the greater the grain radius used the smaller the available cross-section for interaction per unit dust mass. Larger masses of dust are therefore required to fit the same degree of absorption if a larger grain radius is used. This is in contrast to SED radiative transfer modelling where larger grain radii generally result in less dust being required to fit the IR portion of the SED (W15). These two techniques in tandem may therefore provide limits on grain radii for different species or combinations thereof.

It is known that the use of different optical properties may substantially alter dust masses derived using SED fitting for a given species of specific grain radius (e.g. Owen & Barlow (2015)). However, the use of different sets of grain optical constants in our models seems to have only a minor effect on the required dust masses, except for cases where the albedo is close to unity (pure scattering grains).
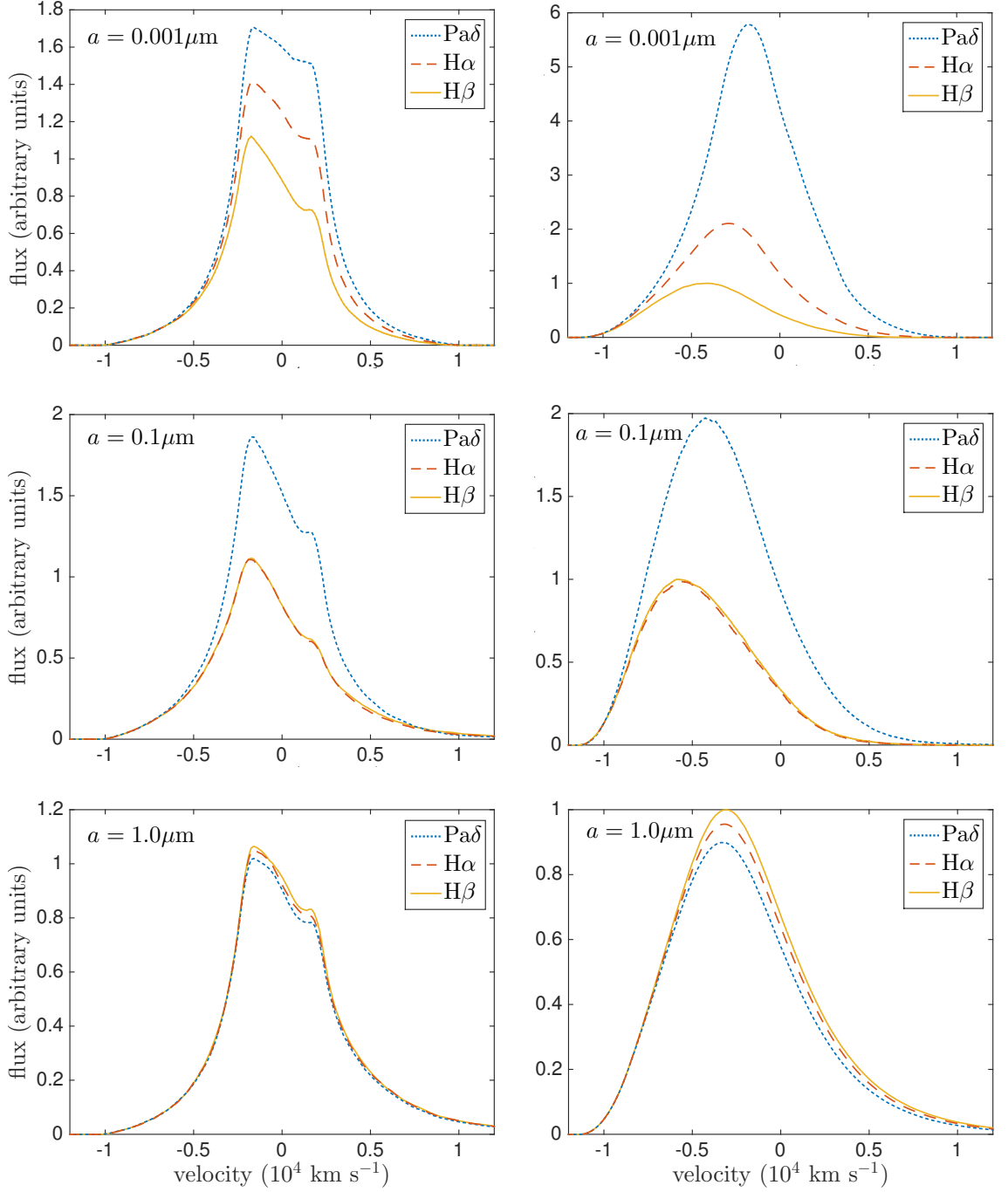
Figure 3.10. Model line profiles for Hα (6563Å in red), Hβ (4861Å in yellow) and Paδ (10049Å in blue) for optically thin and optically thick cases on the left-hand side and right-hand side respectively. All models adopted density profile $\rho(r) \propto r^{-4}$ (i.e. $\beta = 2$), velocity profiles $v(r) \propto r$ and radii ratio $R_{in}/R_{out} = 0.2$. The grain radii used were $a = 0.001$ μm (top), $a = 0.1$ μm (middle) and $a = 1.0$ μm (bottom). All the above models used amorphous carbon.
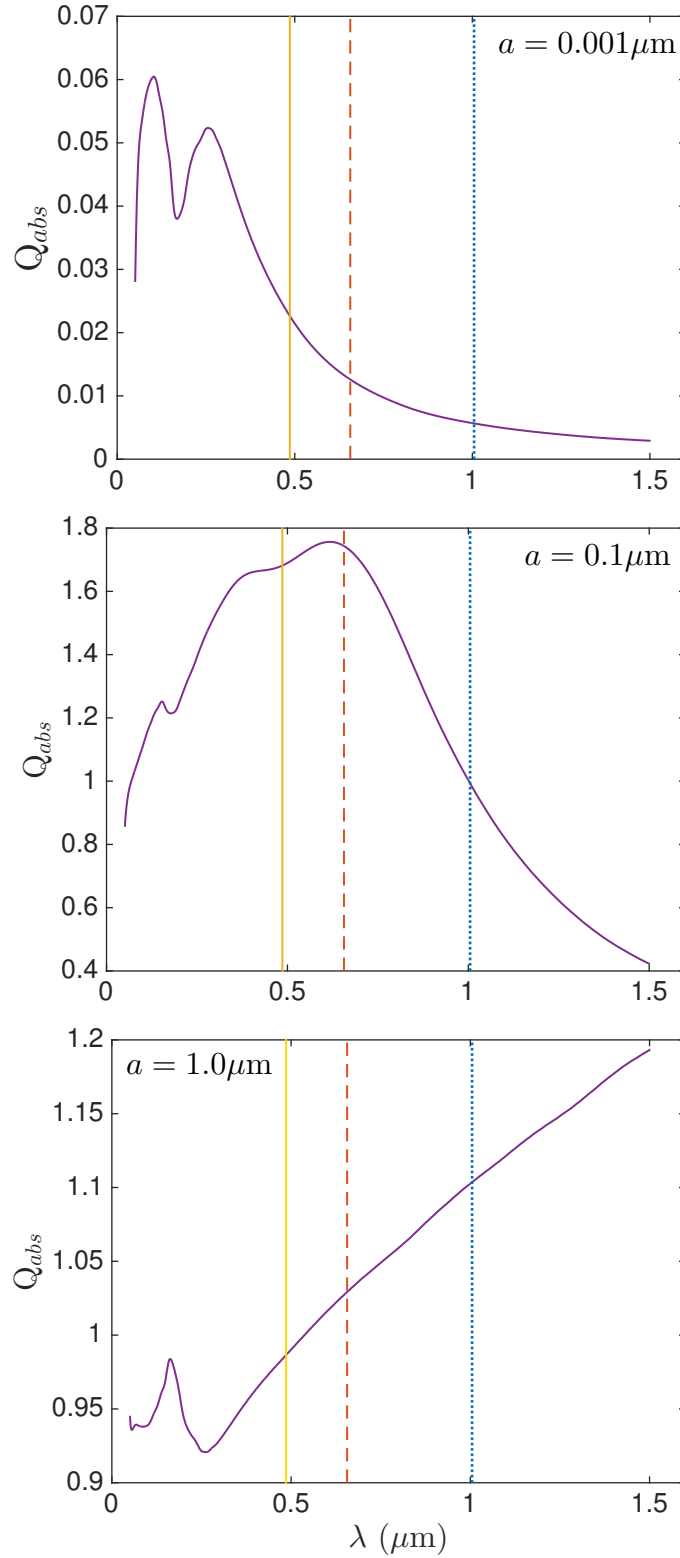
Figure 3.11. The variation of amorphous carbon dust absorption efficiency with grain radius. The grain radii plotted are $a = 0.001$ μm (top), $a = 0.1$ μm (middle) and $a = 1.0$ μm (bottom). The vertical lines mark the wavelengths of Hα (6563Å in red), Hβ (4861Å in yellow) and Paδ (10049Å in blue).

3.2.7 The wavelength dependence of dust absorption

The greater the dust optical depth, the more attenuation of the line there will be. As expected, the red side of the profile suffers a greater degree of absorption than the blue side. The resulting asymmetry is somewhat more complex than perhaps previously thought. Dust has repeatedly been cited as the agent responsible for the apparent blue-shifting of supernova line profiles in the manner of the profiles presented in Figure 3.5; that is, relatively high optical depths result in an overall shift of the entire profile towards the blue. The relationship between the blueshifting of the peaks of profiles and their wavelength has been discussed by several authors in relation to dust formation (Smith et al. 2012; Fransson et al. 2014; Gall et al. 2014).

In practice a relatively large dust optical depth is required to actively shift the peak of the profile bluewards of its natural $-V_{min}$ position (corresponding to the velocity at the inner radius of the shell) unless this value is very small in comparison to V_{max} i.e. the profile originally had a very narrow flat top. In many cases it seems likely that the dust may not be optically thick and the blue-shifting of the peak of the profile is just a result of attenuation in the flat-topped section (close to R_{in}). The peak would then tend to be located at $-V_{min}$.

Since dust absorption is wavelength dependent for $2\pi a < \lambda$, one might expect the position of the peak line flux to be dependent on the wavelength of the line being considered. I note here that whilst variations of the peak velocity of a line as a function of line wavelength may occur in cases of high dust optical depths or small R_{in}/R_{out}, this may not be the case for many supernova lines emitted from ejecta with low dust optical depths. The wavelength-dependence of dust absorption instead can result in differing degrees of extinction in the flat-topped region of each profile but still leave the peak at its blue-shifted position of $-V_{min}$. If this is the case then there would be no reason to expect a variation in the position of the peaks of profiles to be correlated with the wavelength dependence of dust absorption. Instead one would expect it potentially to trace the location of different ions within the ejecta, possibly with different V_{min} values observed for different species.

For lines from the same ion, for example the Balmer and Paschen lines of HI, we might expect to see peaks at the same position but differing degrees of absorption. At high spectral resolutions, it might be possible to detect differences in the shapes of the line profiles, particularly between $-V_{min}$ and $+V_{min}$ where the steepness of the incline traces

the degree of dust absorption. This can be seen in Figure 3.10 where I illustrate the effects of the wavelength dependence of dust absorption for three lines, Hα (6563Å), Hβ (4861Å) and Paδ (10049Å). All lines were modelled using three different grain radii and for both optically thin and thick dust cases. I also show the variation of the absorption efficiency with wavelength for three different amorphous carbon grain radii in Figure 3.11.

3.2.8 The effect of a grain radius distribution

It is important to consider the potential effect on the dust mass of modelling a grain radius distribution instead of a single grain radius. For a grain radius distribution the overall extinction cross section, C_{ext}, at a given wavelength is calculated as

$$C_{ext} = \int_{a_{min}}^{a_{max}} Q_{ext}(a)n(a)\pi a^2 da \tag{3.16}$$

where $Q_{ext}(a)$ is the extinction efficiency for a grain radius a and $n(a)$ is the number of grains with size a. The overall extinction efficiency is then

$$Q_{ext} = \frac{C_{ext}}{\int_{a_{min}}^{a_{max}} n(a)\pi a^2 da} \tag{3.17}$$

The scattering cross-section Q_{sca} is similarly calculated. As a result of these calculations, there is rarely a single grain radius that has the same albedo and extinction efficiency as a size distribution. Modelling a size distribution instead of a single grain radius may therefore alter the deduced dust mass. Since models are only sensitive to the optical depth and the albedo, however, it is not possible to deduce the grain radius range or distribution and only single grain radii are investigated in the models that are presented in the following chapters.

Whilst this apparently limits the scope of these results, it is important to consider the extent to which considering grain radius distributions would alter the derived dust masses. For each model that I construct, I derive a dust mass for a given species at a single grain radius. By considering the equation that determines the optical depth for both a single grain radius and a grain radius distribution, I can approximately calculate the required dust mass for a distribution of grain radii from the properties of a single-size model by equating the optical depths. The optical depth for a single grain radius is proportional to

$$\tau_\nu \propto Q_{ext,\nu}(a)\sigma(a)n_d \tag{3.18}$$

where n_d is the number density of dust grains, $\sigma(a)$ is the cross-sectional area of a grain of radius a and $Q_{ext,\nu}(a)$ is the extinction efficiency for a grain of radius a at frequency ν. On average, this gives

$$\tau_\nu \propto \frac{Q_{ext,\nu}(a)M\pi a^2}{\frac{4}{3}\pi a^3 \rho V} \propto \frac{Q_{ext,\nu}(a)M}{\frac{4}{3}a\rho V} \tag{3.19}$$

for a total dust mass M, total volume of the ejecta V and density of a dust grain ρ.

By equating the equations for the total dust optical depth for a single grain radius and a distribution of grain radii, we obtain (at a specific frequency)

$$M_d = \frac{M_s Q_{ext,s}(a_s)}{a_s} \times \frac{\int_{a_{min}}^{a_{max}} n(a)a^3 da}{\int_{a_{min}}^{a_{max}} Q_{ext}(a)n(a)a^2 da} \tag{3.20}$$

where the subscript s represents the single grain radius quantities and the subscript d represents quantities for the grain radius distribution. This is only calculable for a specific wavelength and is therefore only an approximate conversion when performed at the rest-frame wavelength of the line in question. However, practically, the variation of extinction efficiency and albedo over the narrow wavelength ranges modelled within the code is not significant and so this method produces relatively accurate dust masses (corroborated by running models with the new parameters).

3.2.9 The effect of different species

In the majority of the modelling that follows, a single species, amorphous carbon, is considered. A single species is used since the parameters that affect the quantity of dust required in the model are the albedo and the optical depth. There are therefore likely many possible combinations of species that may result in a good fit to the data. The choice of amorphous carbon is partly motivated by evidence that, for SN 1987A (which, as an incredibly well-observed and local core-collapse supernova, is an excellent test case) the fraction of silicates present in the dusty ejecta is limited to approximately 15% (W15, Ercolano et al. (2007)). It is also motivated by previously published SED models which generally employ amorphous carbon. This is because SED models frequently require far

larger masses of silicate dust than amorphous carbon dust in order to produce similar levels of infrared flux and therefore amorphous carbon models are likely to produce the more conservative dust mass estimates. By modelling with amorphous carbon I may compare directly to these SED models where possible.

I consider the change in dust mass when an alternative medium is used instead of amorphous carbon. I use a generic silicate medium as an illustrative example. In a similar manner to the approach detailed in Section 4.2.6, I may calculate the mass of silicates that is equivalent to an amorphous carbon mass for a single grain radius. I consider the albedo at the original grain radius, calculate the equivalent grain radius for silicates that results in the same albedo and then calculate the new dust mass by considering the change in the extinction efficiency as

$$M_{sil} = M_{amc} \left(\frac{Q_{amc}}{Q_{sil}} \right) \left(\frac{a_{sil}}{a_{amc}} \right) \left(\frac{\rho_{sil}}{\rho_{amC}} \right) \tag{3.21}$$

I will make use of the above "conversion" equations in the next chapter when I consider various models of SN 1987A and discuss the effects of varying both species and grain radius.

3.2.10 The velocity distribution

I do not thoroughly investigate the effects of varying the steepness of the velocity distribution since the influence of this parameter is thoroughly detailed from a mathematical perspective in Section 3.1.1. Simply, the steeper the velocity distribution, the steeper the slope of the sides of outputted line profile. In this sense, there is some degeneracy with the exponent of the density profile. The steepness of the velocity distribution also affects the width of the flat-topped region of the profile via Equation 3.13. One of the primary reasons that this variable is not investigated in more depth is that all models of late-time line profiles from the ejecta of supernovae should adopt a free expansion velocity law $v \propto r$ until the remnant reaches an extremely late stage of its evolution. However, by this point the remnant will likely no longer be visible in the optical or IR.

3.3 Conclusions

Throughout this chapter, I have discussed the various ways in which I tested DAMOCLES against both theoretical line profiles derived from first principles and previously published

models, and have presented example profiles illustrating the excellent agreement between them. For each parameter of interest, I have described the manner in which its variation affects different aspects of the emergent line profile. I have also discussed the effects of altering the properties of the dust itself and have calculated the degeneracies relating to grain radius distributions and composition. This allows for any model with a given set of dust properties to be easily compared to a model with the same intrinsic geometry but with a different dusty medium.

This investigation of parameter space resulted in some very interesting discoveries that may prove important when considering dust formation in the ejecta of CCSNe in the future. Historically, a line profile that was flux-biased towards the blue with a blue-shifted peak was considered to be potentially indicative of dust formation. Whilst this is undeniably the case, it seems likely that a number of other features may also point towards the formation of dust in the ejecta. I have discussed the presence of an extended red-scattering wing and the lack of a need for asymmetry. I have also mentioned the possibility of symptomatically jagged profiles, often with sharp inflection points around the value of the minimum velocity ($\pm V_{min}$). The presence of any or all of these features in the line profiles of the spectra of CCSNe may suggest the presence of newly-formed dust. In addition to these results, the process of exploring parameter space greatly aided me in modelling SN 1987A and the other supernova remnants presented in the following chapters.